Materials Research. 2024; 27(suppl. 2):e20240184
DOI: https://doi.org/10.1590/1980-5373-MR-2024-0184

Al-doped ZnO Thin Films via Sputtering: Influence of Structural Defects on Ozone Gas Sensitivity

Douglas Henrique Sales[a], ***Ramon Resende Leite***[b], ***Julio Cesar Camilo Albornoz Diaz***[b], ***Amanda Akemy Komorizono***[b], ***Maria Ines Basso Bernardi***[b], ***Valmor Roberto Mastelaro***[b], ***Elson Longo***[c], ***Silvio Rainho Teixeira***[a], ***Agda Eunice de Souza***[a]*

[a]*Universidade Estadual Paulista (UNESP), Faculdade de Ciências e Tecnologia, Presidente Prudente, SP, Brasil.*
[b]*Universidade de São Paulo, Instituto de Física de São Carlos, São Carlos, SP, Brasil.*
[c]*Universidade Federal de São Carlos, Laboratório Interdisciplinar de Eletroquímica e Cerâmica, São Carlos, SP, Brasil.*

Received: April 27, 2024; Revised: August 17, 2024; Accepted: August 22, 2024

Nowadays, few studies have reported on the sensitivity of thin films of Al-doped ZnO to ozone. This gas can become harmful to health depending on its environmental concentration. This work presents the sensor response to ozone gas of pure ZnO and Al-doped thin films, prepared by sputtering with varying deposition times. Ceramic targets prepared by SSR, compacted at 65MPa, sintered at 950°C, with densities ranging from 74-97% of the theoretical density, depending on the dopant content were used. The films showed an increase in thickness with deposition time and a preferential growth in the (002) plane of the ZnO structure. Slight changes in the band gap value occurred with increasing Al, whose presence in the ZnO lattice was confirmed by XPS. The sensitivity results to ozone showed that the performance of the films decreased with the Al-doping, which could be attributed to the defects formation related to oxygen in the lattice during Zn-Al substitution or to the greater densification of the films. Although the results showed a decrease in the sensor properties, all films are sensitive to ozone, including the low concentrations of 50 ppb, a limit considered for a maximum daily average for human exposure, established by the WHO.

Keywords: *ZnO, ceramic targets, sputtering, thin films, sensors, ozone.*

1. Introduction

ZnO is an n-type II-VI semiconductor with a hexagonal structure, a band gap around 3.4 eV, and exciton binding energy (electron-hole pairs) of 60 meV[1]. ZnO exhibits properties, such as transparency in the visible spectrum, non-toxicity, electrical, optical, piezoelectric, and catalytic properties. In addition, chemical stability, material availability, and low cost are also observed in this material. With this range of characteristics and multifunctional properties, ZnO presents several potential applications in micro and optoelectronics. When arranged in the thin film form, ZnO can be used, for example, in resistive coatings and UV photodetectors, gas sensors, photocatalysis, and as transparent conducting oxides (TCOs) for photovoltaic cells, among other applications[2]. The properties of ZnO can be enhanced through doping with other elements, depending on the applications. In the literature, many studies are dedicated to investigating ZnO thin films with controlled dopings, such as In[3-5], Ga[6,7], Al[8,9], Ag[2], Cu[10], and Co[11]. These elements can replace Zn in the lattice, altering or enhancing optical or electrical properties. Each dopant acts uniquely in the structure, aiming for pre-established applications for the final Zn compound. Doping with Al, for example, can alter the optical characteristics of ZnO films, such as the band gap energy, improving the transmittance of the films, which imparts an important feature for potential applications in photovoltaic cells[12]. Additionally, these elements can be introduced in combination (co-doping) into the ZnO structure[13]. Doping or co-doping, therefore, influences the physical and chemical characteristics of ZnO films, expanding their technological applications. For example, Fe and Al:co-doping ZnO films can increase carrier concentration and electron mobility, which are important parameters for applications in spintronic and optoelectronic devices[14]. When co-doped with Ga and Mg under certain conditions, the resistivity of ZnO thin films can decrease, enhancing their resistance to humidity[15], which is a relevant feature for applications in gas sensors and solar cells.

Regarding the application in sensors for toxic and non-toxic gases, aluminum-doped zinc oxide (AZO) has been one of the compounds evaluated in recent years, due to its properties modified by the dopant aluminum[16,17]. The high mobility of bulk conduction electrons, thermal and chemical stability, and energy structure are examples of properties that can be highlighted, favoring applications such as gas sensors.

---

*e-mail: agda.souza@unesp.br

Although the properties of ZnO and AZO films are known and still under study, current research on gas sensors needs to be conducted primarily to seek improved performance for the sensitivity of thin film gas sensors, and expand their limits, and gas detection spectrum. This enhancement in the sensitivity of gas sensors based on ZnO is of great importance, both from an industrial and domestic standpoint for the detection of hazardous and explosive gases, including LPG, as from a medical perspective for detecting toxic gases harmful to health.

Many deposition methods for thin films of Al-doped ZnO have been utilized. Among the various deposition methods, spray pyrolysis[17,18], sol-gel[9], dip coating[19], organometallic chemical vapor (MOCVD)[20,21], pulsed laser deposition[22], and RF or DC magnetron sputtering[23-30], stands out. Among these methods for preparing thin films, magnetron sputtering deposition is a well-known and efficient technique for thin film quality formation, in addition to easy industrialization. The magnetron sputtering thin-film deposition method offers numerous advantages over the above deposition techniques. Among these advantages, the uniformity of the deposited films and the thickness precision, achieved by adjusting deposition parameters, stand out. It allows the deposition of films from various materials, such as ceramic or refractory materials, including multilayers with the same uniformity and thickness controls. The deposited films exhibit better adhesion to the substrate (which can be made of different materials and with different geometries), higher densification, and low contamination rates due to the vacuum in the deposition process. Moreover, it can be easily scaled for industrial use, where the properties of the films can be controlled and adjusted by varying and controlling the deposition parameters[31-33].

In the sputtering deposition method for thin films, a bombardment of the target with positive atoms or ions (usually from an inert gas), causes the atoms ejection from the target that condenses onto a substrate. When thin films are prepared using this method, the optical and electrical properties are influenced not only by the deposition parameters (vacuum, sputtering gas pressure, substrate, and target temperature, etc.) but also by the characteristics of the sputtering targets, especially by variations in their composition[34]. It is common in the literature to find works that emphasize the behavior of thin films deposited by this technique, such as transmittance in the visible region, morphology, and carrier mobility[35-37]. However, few works report the importance of the prior target preparation, when is processed for use in the sputtering deposition of high-performance films.

To obtain ceramic targets suitable for the sputtering process, precursor powders must undergo processing before being molded into target form. Similarly, the targets require appropriate heat treatments to exhibit the essential characteristics for a good thin film preparation[38].

In this work, ceramic targets of ZnO and Al-doped ZnO were produced via solid-state reaction to be used in the magnetron sputtering process. From these ceramic targets, thin films were produced for applications in ozone gas sensors, considering the lack of literature reporting the sensitivity of this gas using thin films of these materials. Ozone gas detection (colorless, with a characteristic odor, and explosive) is important because it is an atmospheric pollutant capable of causing health problems, including those related to respiratory systems, especially if found in high concentrations. In places where ozone is used or produced as part of industrial processes, its monitoring is important to ensure the safety of workers, preventing excessive exposure to this gas. Korotcencov and Cho[39] had already mentioned in their work that, according to the World Health Organization (WHO), the air quality guideline for ozone should be set at 100 μg/m^3 (~50 ppb) for a maximum daily average of 8 hours, and these values have not currently been changed. According to the authors, exposure to 0.1–1 ppm causes headaches, eye irritation, and respiratory tract irritation. An individual who stays for two hours in an environment containing 0.1 ppm of ozone will experience a 20% loss in respiratory capacity, and after remaining in places for 6 hours with an atmosphere containing 1 ppm of ozone, will suffer from bronchitis attack. Therefore, detecting ozone levels in the air using thin film-based sensors can help protect people's health, as implement pollution control measures. Then, it is in this context that we present, in this study, an investigation into ozone gas detection, including low concentrations, using sensor films prepared by magnetron sputtering from ZnO ceramic targets, also evaluating the influence of Al dopant on sensor properties.

2. Materials and Methods

2.1. Preparation and characterization of ZnO and AZO targets

ZnO and Al-doped ZnO targets with 1, 2, and 3 mol% of Al (ZnO, AZO1, AZO2, and AZO3, respectively) were prepared by solid-state reaction, using commercial ceramic powders (ZnO, Sinthy, 99% purity, and Al_2O_3, Alfa Aesar, 99% purity). Both precursors (ZnO and Al_2O_3) were dry-milled separately in a ball mill with zirconia balls (~5 mm in diameter) for 12 hours. The ceramic powders were placed in closed containers, occupying about ¼ of the volume, with balls occupying half of the container volume. After the milling process, the powdered precursors were dried in an oven at 100°C for 24 hours and then used for the ceramic target production. The targets were uniaxially pressed in a 58mm diameter mold using a Marcon press with a compaction pressure of 65 MPa for 1 minute. Subsequently, they were heat-treated using a Jung furnace with a heating ramp of 3°C/min up to 700°C for 1 hour, followed by another ramp of 3°C/min up to 950°C, and maintained at this temperature for 6 hours.

The targets were characterized by X-ray diffraction (XRD) using a Shimadzu XRD-6000 equipment with a $CuK_{\alpha1}$ (λ = 1.5406Å) and $CuK_{\alpha2}$ (λ=1.5444Å) radiation source, operated at 40kV and 30 mA. Diffraction data were analyzed according to the Powder Diffraction File™ database (PDF) of the International Center for Diffraction Data (ICDD). Scans were performed over an angular range of 10º to 80º (2θ) at a scanning rate of 2º/minute. The ceramic targets (ZnO and AZO) were characterized for chemical composition, in oxides %, by the X-ray fluorescence (XRF) in a qualitative-quantitative mode, in a vacuum, using a Shimadzu XRF-700 system.

This equipment has a scanning range from Sodium (Na) to Scandium (Sc) and from Aluminum (Al) to Uranium (U). The primary radiation source is a Rhodium (Rh) cathode, directed through a 10 mm diameter collimator. Additionally, the apparent density of the targets was conducted using the Archimedes method.

2.2. Preparation and characterization of ZnO and AZO thin films

The ZnO and AZO ceramic targets were employed for thin film production using an ORION 5 AJA International magnetron sputtering system. The films were deposited onto glass and silicon substrates utilizing radio frequency (RF) power of 80W, with a controlled working pressure of approximately 3 mTorr (0.3 Pa), without chamber heating. Argon (Ar) was used as the inert sputtering gas, with a flow rate of 15 sccm (standard cubic centimeters per minute). The substrates were rotated at 60 rpm during the deposition process at 30, 60, and 120 minutes. The substrates were placed at a fixed distance of 18 cm from the target inside the chamber. All films were prepared in a single layer and without substrate heating. The substrates used (soda-lime glass and silicon) were previously cleaned with acetone using ultrasound for 20 minutes and dried in an oven for 60 minutes.

The films were characterized by X-ray diffraction (XRD) using a Shimadzu XRD-6000 instrument; thickness measurements using a Veeco profilometer, Dektak 150, with measurements taken at five different regions of each film; X-ray photoelectron spectroscopy (XPS), utilizing a Scienta Omicron ESCA+ spectrometer with Al-K$_\alpha$ X-ray monochromatic source (hν = 1486.6 eV); ultraviolet-visible (UV-Vis) absorption spectroscopy using a Shimadzu UV-2600 spectrophotometer, scanning from 200 to 850 nm. The absorbance results were used to determine the optical band gap (Eg) of ZnO and AZO using the Wood and Tauc method[40]; the films were characterized by scanning electron microscopy (SEM) using a Sigma Zeiss FEG instrument; the surface roughness of the films deposited for 30 min was analyzed using atomic force microscopy (AFM) with a Park Systems - NX10 instrument.

Sensitivity measurements to ozone gas were performed with the films deposited for 30 min on silicon electrodes with an interdigitated gold circuit, heated to 250°C and exposed for 10 min to a gas flow of 100 sccm at concentrations of 50, 230, 390, and 570 ppb, with a recovery time of 20 min approximately.

3. Results

3.1. ZnO and AZO target

Figure 1 shows the X-ray diffraction (XRD) results of the ZnO, AZO1, AZO2, and AZO3 ceramic targets. Peaks corresponding to the ZnO with wurtzite phase were identified, with a hexagonal structure characterized by two interlinked sublattices of Zn^{2+} and O^{2-} ions, where each Zn^{2+} ion is surrounded by a tetrahedron of O^{2-} ions, and vice versa. This tetrahedral coordination gives rise to polar symmetry along the hexagonal axis. This polarity is responsible for some properties of ZnO, besides being the main factor in crystal growth and defect generation[41]. The results also show that targets containing 2 and 3 mol% of Al (AZO2 and AZO3) exhibit the beginning of the secondary phase formation of the spinel-type zinc aluminate ($ZnAl_2O_4$), with a cubic structure, characterized by low-intensity peaks. The natural form of this compound is known as gahnite, in which the Zn atoms have a tetrahedral configuration. In contrast, the Al atoms occupy octahedral sites in a face-centered cubic (FCC) lattice of oxygen atoms[42]. The $ZnAl_2O_4$ is a phase of interest in some ceramics, depending on the applications, as it has a wide band gap (~3.8 eV), which gives it photoelectronic, optical, and dielectric properties, as well as high thermal and chemical stability. With these properties, materials containing $ZnAl_2O_4$ are widely applied in photocatalysis, sensors, high-temperature ceramics, dielectrics, and optoelectronic electrodes, among others[43,44]. Fang et al.[45] observed the $ZnAl_2O_4$ phase formation in AZO targets prepared by SSR between ZnO and Al_2O_3 at 1300°C. Despite the $ZnAl_2O_4$ phase precipitation, the AZO films deposited via sputtering using this target did not show the presence of this phase, which did not demonstrate changes in the properties of the deposited films. These results are opposite to those presented in the work of Wei et al.[35]. Mallick et al.[46] also observed the $ZnAl_2O_4$ spinel phase in AZO targets from 900°C. However, XRD peaks corresponding to this phase were also not observed in the films deposited with the targets, although the authors noted indications of a secondary phase through XPS measurements. In our XRD results, the presence of Al is only observed in the precipitation of this secondary phase. In the peaks corresponding to the ZnO phase, it is not possible to affirm the presence of Al^{3+} as a substitutional cation for Zn^{2+} or interstitial in the wurtzite crystal lattice. However, a few changes in the intensities corresponding to this phase in the AZO films have been observed in Figure 1.

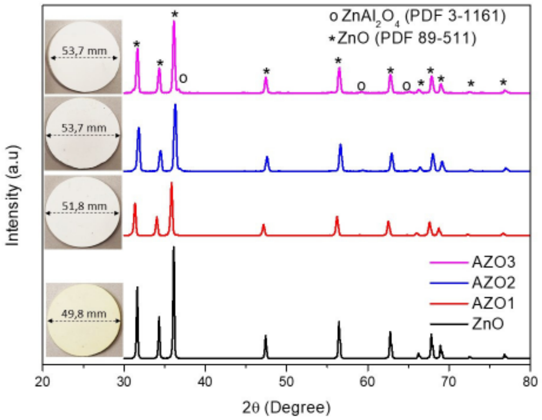

Figure 1. X-ray diffraction patterns of ZnO and AZO ceramic targets, sintered at 950°C.

Table 1 shows the apparent density (AD) results of the ceramic targets, pressed at 65 MPa and sintered at 950°C. It is noted that the AD decreases with the dopant content. In addition to AD, the values related to the theoretical density (TD) of each compound of the targets are also shown, considering the theoretical density of ZnO as 5.67 g/cm^3 and Al_2O_3 as

Table 1. Density, diametrical shrinkage, and chemical composition of targets prepared by SSR pressed at 65MPa and sintered at 950°C.

Target	AD (g/cm^3)	AD concerning TD (%)	Diametrical shrinkage (%)	Chemical composition (oxides %)		
				ZnO	Al_2O_3	Others
ZnO	5.5	97.3	16.2	99.690	-	0.310
AZO1	4.9	86.9	11.8	97.984	1.713	0.303
AZO2	4.3	76.2	7.9	97.069	2.700	0.231
AZO3	4.1	74.1	7.9	95.720	3.928	0.352

3.98 g/cm^3. It is observed that the AD values were above 74% concerning the TD. Wang et al.[47] observed an increase in density (relative to TD) of AZO2 target sintered at 1100°C as a function of time variation. The target prepared by the authors, with a pressure of 35MPa, showed values ranging from ~92 to 95% of the TD. Garcia-Salínas et al.[9] prepared ZnO and AZO1 targets from previously synthesized ceramic powders. The authors used a compression pressure of 16MPa and a sintering temperature of 1000°C, obtaining density values of 95% for the ZnO targets and 93% for the AZO1 targets, relative to the TD. Asemi et al.[36] found around 98.9% of the TD. However, the processing of the AZO2 targets prepared by the authors differs from ours and other works, that is, they were pressed at 30MPa and sintered at 900°C under low and high vacuum pressure. Other studies have also shown values above 97% of the TD using alternative methods for target processing and sintering[48]. It is noted, therefore, that there is a significant variation in methods for preparing ZnO and AZO ceramic targets, each with its peculiarities resulting in different densities, but all viable for use in sputtering film deposition.

About the diametrical shrinkage suffered by the targets, we observed a greater shrinkage for the ZnO targets. As the Al dopant is added, the diametrical shrinkage percentage of the targets decreases, meaning that the shrinkage follows the density of the targets. The lower the shrinkage, the lower the density of the targets. This variation may be associated with the chemical characteristics of the bonds between Zn–O and Al–O during diffusion in the SSR process, in addition to the grain growth kinetics[48].

Table 1 also presents the major chemical composition of the ceramic targets (oxides %). It can be observed that the predominant stoichiometry (ZnO and Al_2O_3) for the doped targets (AZO1, AZO2, and AZO3) slightly deviates from the initially calculated values. In addition, a percentage of minor oxides, which include Nd_2O_3, CuO, Cr_2O_3, MnO, V_2O_5, Yb_2O_3, Pr_6O_{11}, Sm_2O_3, and CeO_2, were observed at low concentrations to all targets. These impurities may have resulted from the precursors initially used, or contamination during the target production process.

3.2. ZnO and AZO thin films

Figure 2 shows the thickness of the films and the deposition rate as a function of time. In general, it is observed that the thickness increases with the deposition time of the film, as expected; however, it decreases with the percentage of Al in the ZnO lattice. About the deposition rate (*insert*), it is observed that there is a reduction in the rate as the Al dopant increases in the ZnO host lattice. The lowest deposition rate values are observed in the AZO2 and AZO3 films. This behavior may be related to higher Al–O bond energy, which can also be influenced by the excess of Al in the lattice of the ceramic target compounds, as observed in their chemical analysis (Table 1). Considering that the deposition parameters (power, gas flow) were kept constant for all films, there may have been insufficient energy to remove atoms from the AZO2 and AZO3 targets, during the deposition process. Another factor that may have influenced is the presence of the $ZnAl_2O_4$ secondary phase in these ceramic targets, which may have precipitated on the surfaces, inhibiting the process of removing Al and Zn atoms from the wurtzite phase of the target[35]. By varying the time, a reduction in the deposition rate at 60 minutes is observed compared to 30 minutes for all samples. For the 120-minute deposition time, the deposition rate increases again smoothly, except for sample AZO2. Apparently, in this case, the removal of Zn and Al atoms from the target was more effective, compared to the 60-minute time.

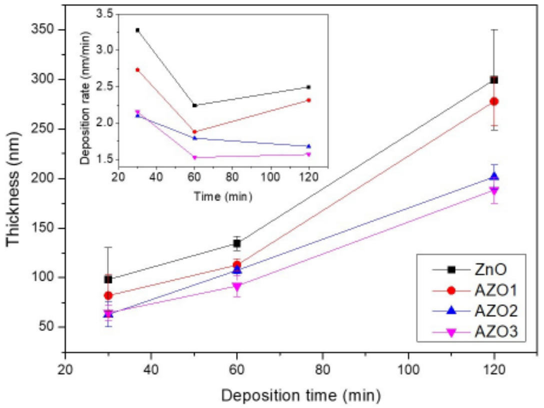

Figure 2. Thickness and deposition rate of ZnO and AZO films.

Figure 3 presents SEM images of the films cross-section and the estimated thicknesses, obtained according to the scale of each image. It is observed that the values found are consistent with those determined by profilometry, although some variations were noted. The most divergent values were those for the AZO1_60 film, where the cross-sectional measurement was ~59 nm higher than the measurement obtained by profilometry, and the AZO2_120 film, where the image showed a difference of ~49 nm greater than that obtained in the profilometry measurement. It is also observed that for the films deposited in 60 minutes, where the deposition rate is considerably reduced (see Figure 2 *inset*), the cross-

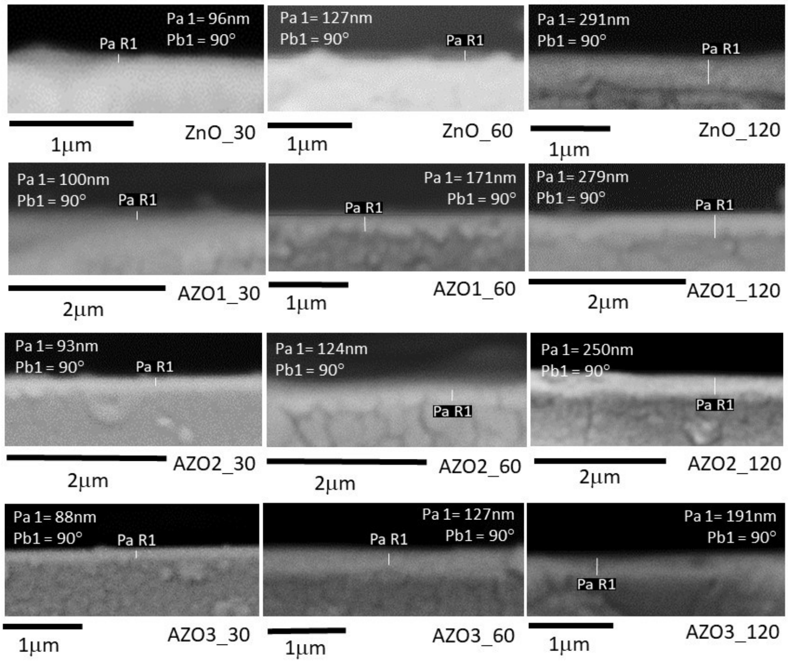

Figure 3. SEM images of ZnO and AZO films cross-section.

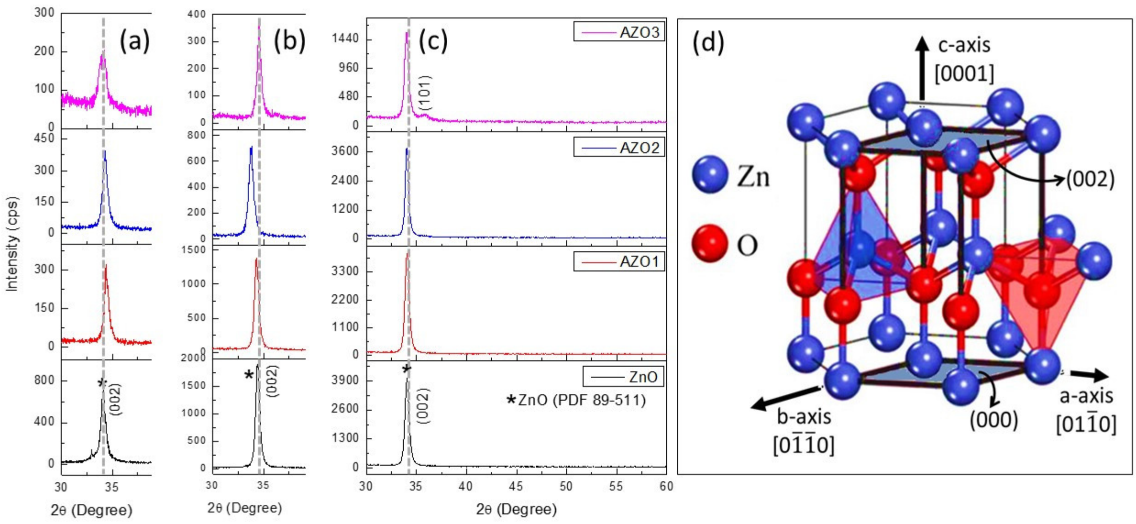

Figure 4. X-ray diffraction patterns of films deposited on a glass substrate: (a) 30 min; (b) 60 min; (c) 120 min; and: (d) Wurtzite structure illustration.

sectional images of the films are not sharp, suggesting variations in the densification of ZnO and AZO particles grown on the substrate. In general, it can be stated that the film thicknesses observed in the cross-sectional images increase with deposition time, confirming the data obtained by profilometry (Figure 2).

Figure 4 shows the diffractograms of the films deposited on glass substrates at different deposition times. A peak at $2\theta \approx 34°$ was observed for all films, indicating growth with preferential orientation in the corresponding plane (002), along the c-axis of the wurtzite structure, perpendicular to the substrate, as observed in other literature works[26,49]. The oriented growth in the (002) plane of ZnO (parallel to the (000) plane shown in Figure 4 (d)) occurs due to its lower surface energy compared to other planes, and for this reason, the growth rate in this direction is faster than in other directions[36]. It is also observed that the intensity of the diffraction peaks decreases with the increase in the dopant Al content, with some exceptions, showing little or no peak shift. Kumar et al.[29] reported that when a peak corresponding to the (002) plane shifts to lower angle values (2θ), Al^{3+} may have occupied an interstitial site in the lattice. Furthermore, since Al^{3+} has a smaller ionic radius than Zn^{2+}, the diffraction peaks should shift to lower angle values. This behavior was observed for the AZO1 and AZO2 samples deposited for 60 min (Figure 4 (b)).

It is important to mention again that although a secondary phase $ZnAl_2O_4$ in the AZO2 and AZO3 ceramic targets used in the film deposition have precipitated, the films remained monophasic. Wei et al.[35] reported that the $ZnAl_2O_4$ phase may segregate on the ceramic target surface, reducing the Al content on the surface available for the sputtering deposition process. Despite this, the AZO phase also grows oriented in the (002) plane, dominated by the wurtzite structure. In these cases, the diffusion of Al for the growth of AZO films, with Al^{3+} replacing Zn^{2+} in the lattice, occurs from the substrate surface. Additionally, the difference in ionic radius between Al^{3+} (0.535 Å) and Zn^{2+} (0.740 Å) would result in a contraction of the crystal lattice in the case of Zn/Al substitution, thus leading to a decrease in interplanar spacing. Consequently, this causes the displacement of the (002) peak to higher angle values (2θ), as observed in some films shown in Figure 4. These results suggest, therefore, that interstitial occupation or substitution of Zn^{2+} by Al^{3+} in the crystal lattice of the deposited films can simultaneously occur, regardless of the presence of the $ZnAl_2O_4$ secondary phase in the targets (AZO2 and AZO3). The peak shift also indicates changes in the lattice parameter resulting from the Zn/Al substitution[50].

It is also observed that, for the AZO3 films deposited in 120 min, a low-intensity peak corresponding to growth on the (101) plane of the wurtzite phase was identified. This behavior suggests that the growth of polycrystalline AZO may be influenced by the film thickness resulting from the deposition time.

Based on the results of XRD of the deposited films, the average crystallite size was determined using the Scherrer equation (equation 1). In this equation, λ is the wavelength of the X-ray (1.5406Å), θ is the Bragg angle (in radians) corresponding to the crystallographic plane (002), β is the full width at half maximum (FWHM) of the X-ray diffraction peak of highest intensity (in radians), and K is a constant corresponding to the shape factor, which varies with the particle geometry. Generally, a 0.9 value is used, considering particles with geometry close to spherical. To determine the average crystallite size, it is necessary to correct the Bragg peak, using, for example, a reference sample, such as silicon. Thus, the full width at half maximum of the Bragg peak (β) is given by equation 2, where β_a corresponds to the full width at half maximum of the diffraction peak of the sample, and β_b to the full width at half maximum of the diffraction peak of a standard sample[28]. It is worth noting that the crystallite size is the size of a single crystal within a particle or grain.

$$D = \frac{K\lambda}{\beta cos\theta} \tag{1}$$

$$\beta^2 = \beta_a{}^2 - \beta_p{}^2 \tag{2}$$

Based on the results shown in Table 2, the average crystallite size (D, in nm) for all films increases with the deposition time, that is, with the film thickness of all samples. Concerning the dopant, an increase in the average crystallite size is observed, when doped with 1 mol% of Al, for all deposition times. From there, i.e., for samples with 2 and 3 mol% (AZO2 and AZO3), the average crystallite size decreases again for all deposition times. Table 2 also presents the dislocation density values, calculated using equation 3. Dislocation density (δ), also known as displacement density or defect density refers to the concentration of dislocations in a crystal matrix, which describe imperfections or deformations in the positions of the atoms in a crystal[37]. Therefore, it is determined as a function of the average crystallite size (D). Dislocation density corresponds to the number of imperfections per unit area or volume. For the case of AZO films, the dislocation density per unit area was determined (equation 3).

$$\delta = \frac{1}{D^2} \tag{3}$$

It is observed that the dislocation density decreases with deposition time, i.e., with increasing film thickness, for all films. This behavior may be related to the accommodation or relaxation of the lattice over time, which promotes a decrease in defect density as the crystal grows[29]. This result

Table 2. Average crystallite size, dislocation density, microstrain, and lattice parameter *c* of AZO films.

Films	Deposition time (min)	D (nm)	δ ($\times10^{-3}$ nm^{-2})	ε ($\times10^{-3}$)	c (Å)
ZnO	30	6.3	24.8	1.9	5.2752
	60	9.3	11.4	1.3	5.2722
	120	35.3	0.80	0.3	5.2572
AZO1	30	8.8	12.9	1.3	5.2662
	60	45.4	0.48	0.3	5.2572
	120	207.6	0.02	0.006	5.2498
AZO2	30	9.4	11.2	1.3	5.2842
	60	29.9	1.11	0.4	5.2752
	120	81.1	0.15	0.2	5.2572
AZO3	30	9.5	11.2	1.3	5.2662
	60	11.5	7.54	1.0	5.2842
	120	38.3	0.68	0.3	5.2572

is consistent with the crystallographic behavior of the films observed in the X-ray diffraction patterns (Figure 4). It is noted that all samples exhibit increasing peak intensity as the deposition time increases, indicating films with greater long-range structural atom organization and a decrease in lattice imperfections density, accompanied by an increase in the average crystallite size[37]. Concerning the dopant variation there is no direct correspondence with the Al content in the lattice. This random behavior may be related to the sites where Al occupies in the ZnO crystal lattice (substitutional or interstitial), which may limit the crystallite growth due to the binding energies involved.

Table 2 also presents the microstrain (ε) results, determined using equation 4, where β corresponds to the full width at half maximum of the Bragg diffraction peak, and θ corresponds to the angle of this diffraction peak[51].

$$\varepsilon = \frac{\beta}{4tan\theta} \tag{4}$$

Microstrain corresponds to small variations in the crystal lattice, arising from point defects such as Zn/Al substitution or interstitial Al. The microstrain in the crystal lattice of AZO films can result in internal stresses distributed throughout the material, but they are insufficient to cause macroscopic deformations. On the other hand, microstrain can influence the physical properties of the films, such as their optical properties and gas detection sensitivity. As shown in Table 2, the microstrain (ε) decreases with the deposition time of the films, as does the dislocation density (δ). This result suggests that deposition time is a parameter that directly influences the accommodation of deposited particles, minimizing variations and defects in the crystal lattice of the films. When these results are examined in relation to the increase of Al in the lattice, it cannot be stated that there is a direct correlation. However, in some cases, a decrease in microstrain with the increase of Al can be observed. In these cases, the presence of Al may influence these local (ε) and linear (δ) defects, primarily due to the difference in its ionic radius compared to the ionic radius of Zn (Zn^{2+} = 0.740 Å and Al^{3+} = 0.535 Å)[33] This difference in ionic radii also influences the lattice parameter *c* of the AZO compound that forms the films[33]. Note that the lattice parameters of the AZO1 films are smaller than those of the ZnO films at all deposition times. On the other hand, the AZO2 and AZO3 films show a slight increase in the lattice parameter *c* compared to the ZnO and AZO1 films. In these cases, other factors may have influenced this lattice expansion. Das et al.[52] explain that, based on the theoretical density of states studies, the average bond length along the *c* axis between O and Zn, located near a substitutive Al ion, is greater than the Zn–O bond length in an undoped structure. In our case, the higher Al content in the AZO2 and AZO3 films lattice has certainly contributed to this expansion in the Zn–O bond, as opposed to the differences in ionic radii (Zn/Al), which had a predominant influence on the AZO1 films. We also observed an inverse relationship between the lattice parameters and the corresponding average crystallite size. These results suggest that lattice expansion is a limiting condition for the growth of crystallites in AZO2 and AZO3.

The lattice parameter *c* of the ZnO and AZO films with a hexagonal structure, shown in Table 2, was determined using the (002) plane of the diffraction peak observed in the films diffractograms (Figure 4). The lattice parameter calculation was based on Bragg's Law and performed using equation 5[53,54].

$$\frac{1}{d^2} = \frac{4}{3}\left(\frac{h^2 + hk + k^2}{a^2}\right) + \frac{l^2}{c^2} \tag{5}$$

Figure 5 shows the XPS spectra of the AZO films deposited for 60 min. The results shown in Figure 5 (a) are characteristic energy peaks of Zn, O, and C. For films containing Al in the ZnO lattice, there are also indications of the Al energy peak. A charge correction was applied to all XPS spectra by adjusting the binding peak energy of carbon C 1s at 284.6 eV. The presence of Al is confirmed by Figure 5 (b), where a smooth peak at ~74 eV corresponding to Al 2p is shown, suggesting the incorporation of Al^{3+} into the Zn^{2+} sites of the ZnO lattice[19,55].

Figure 6 shows Zn $2p_{3/2}$, Zn $2p_{1/2}$, and O 1s XPS spectra for all films. It can be observed that the peaks corresponding to Zn $2p_{3/2}$ and Zn $2p_{1/2}$ (Figure 6 (a), (c), and (e)) do not show significant changes, indicating that the oxidation state of Zn is 2+. Additionally, the energy difference between them, which corresponds to ~23 eV, is typical of the wurtzite structure[56]. Regarding the binding energy of O 1s for the ZnO film (Figure 6 (b)), three peaks were fitted at 530.5 eV, 531.7 eV, and 532.7 eV. According to Namgung et al.[55], the origin of these three peaks of O 1s is, respectively, from the oxygen atoms in the lattice of the hexagonal wurtzite structure of ZnO (i.e., O^{2-} ions and tetrahedrally coordinated Zn^{2+} ions, as shown in the *inset* of Figure 6 (b)), oxygen ions (O^- or O^{2-}) in regions with oxygen deficiency, and atoms bonded to the surface of ZnO. With the Al^{3+} doping, the configuration of the O 1s peaks reduces to two (~531 eV and 532 eV), shifting smoothly to higher values with the increase of Al content in the ZnO lattice (**Figure 6 (d)**, **(f)**, and **(h)**). This behavior may be related again to the presence of Al^{3+} in the Zn^{2+} at sites of the ZnO lattice. The valence mismatch between these elements in the lattice generates a concentration of oxygen point defects (oxygen vacancies and/or interstitial oxygen, as shown in the inset of Figure 6 (d) and 6 (f), respectively), which, in turn, should increase with the Al content, gradually raising the binding energy with oxygen[19]. These XPS results, therefore, confirm the presence of Al^{3+} in the Zn^{2+} site in the ZnO lattice. However, this substitution may be partial, considering the XRD results that suggest the presence of Al^{3+} in interstitial sites. Although the XPS characterizations were performed only for the films deposited in 60 minutes, the results can be extended to the other films.

Figure 7 shows the UV-Vis absorbance results as a function of photon energy for the films deposited during 30, 60, and 120 minutes, respectively. The Eg values were determined using the method proposed by Wood and Tauc (1972)[40], according to Equations (6) and (7). In these equations, *h* represents the Planck constant, ν is the radiation frequency (UV-Vis), *n* indicates the type of electronic transition between bands (direct transition (*n* = ½) for ZnO), and α is a constant

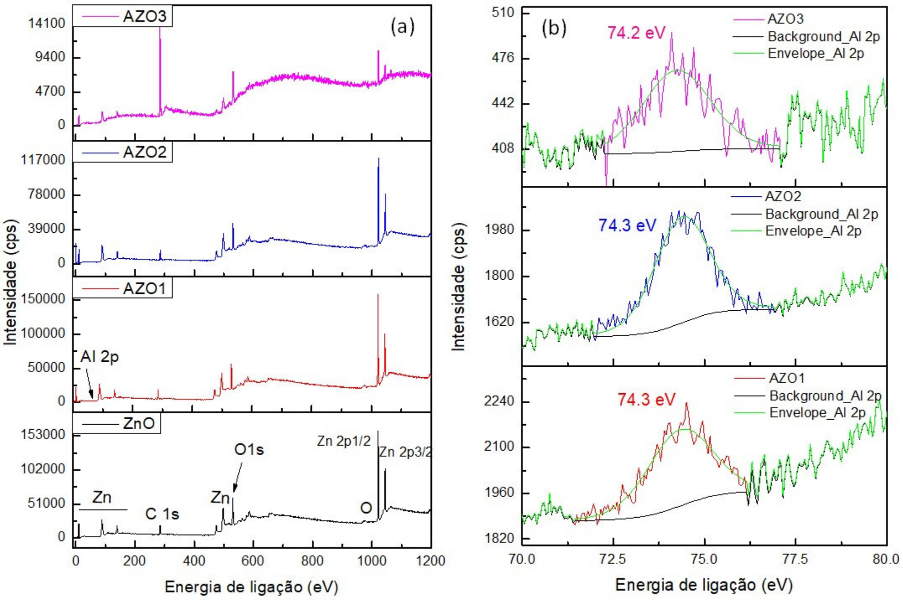

Figure 5. X-ray photoelectron spectra of ZnO and AZO films deposited for 60 min: (a) Survey; (b) Al 2p.

or absorption coefficient, which was determined based on the absorbance (*A*) and the thickness of each film (*t*)[25].

$$h\nu\alpha = \left(h\nu - E_g\right)^n \quad (6)$$

$$\alpha = 2,303.\frac{A}{t} \quad (7)$$

It is observed that Eg varies from 3.20 eV for ZnO to 3.40 eV for the films containing Al. There is no direct relationship between the band gap value and the deposition time, i.e., the thickness of the film. On the other hand, with the increase in the Al percentage in the ZnO lattice, a slight increase in the Eg is observed. This slight increase has also been observed in other works in the literature[57]. There are reports that this increase in Eg values as a function of Al adding to the ZnO host lattice is related to the so-called Burstein-Moss effect, a phenomenon observed in semiconductors when the concentration of free carriers is increased[35,58]. This fact agrees with the conditions exhibited by the AZO films. Zn^{2+} by Al^{3+} substitution, as mentioned earlier, causes a charge destabilization, which may contribute to an increase in the number of carriers at the substitution site. With this, the Zn conduction band can be filled up to an energy level close to the upper limit of the forbidden band, causing a slight expansion. On the other hand, a decrease in the band gap values with the increase of Al content in the lattice in films prepared by the other deposition methods, such as spin coating, has already been reported[59].

Figure 8 shows the SEM images of the film surfaces deposited for 30, 60, and 120 minutes, and AFM images of the films deposited for 30 minutes. The SEM images reveal well-defined grain boundaries and variations in particle size, particularly in the ZnO film. With the increase in deposition time from 30 to 60 minutes, thus increasing the thickness of each film, a slight increase in the average grain size is observed. This grain size does not show significant changes with the increase in deposition time to 120 minutes. Notably, the AZO1_120 films exhibit a more homogeneous surface than those AZO1 films deposited in 60 minutes. On the other hand, with the increase in the dopant Al percentage, there is a decrease in this grain size, leading to an increase in film density. The decrease in grain size due to the presence of Al in the ZnO lattice can therefore lead to a reduction in the charge carriers transmission at the grain boundaries, and, consequently, the electrical properties of these films will be altered[28]. The AFM images of a 1 μm^2 area on the surface of the films deposited in 30 minutes suggest an apparent growth perpendicular to the substrate surface, which agrees with the DRX results already discussed. The RMS roughness of the films varies smoothly, from 1.6 to 1.9 nm, with the increase in Al content in the lattice. These values are lower than some found in the literature for ZnO and AZO films deposited by RF or DC sputtering using ceramic targets[25,56] or other techniques[60,61]. It is observed that the roughness increases with the decrease in grain sizes. As discussed earlier, ZnO films exhibit a wider variation in deposited grain sizes, which may aid in packing, resulting in lower roughness. These factors may be related, to the deposition rate and film thickness. As discussed, film thickness and the deposition rate decrease with the Al percentage in the ZnO lattice (Figure 2). Therefore, by depositing fewer molecules per minute, fewer grains or smaller grains will be produced with less size variation, which, in turn, will irregularly aggregate, increasing the surface roughness of the Al-containing films (AZO). When compared to the results for average crystallite size and lattice parameters (Table 2), a direct relationship with grain size is observed in the SEM images in Figure 8. With the increase of deposition time from 30 to 60 minutes, the average

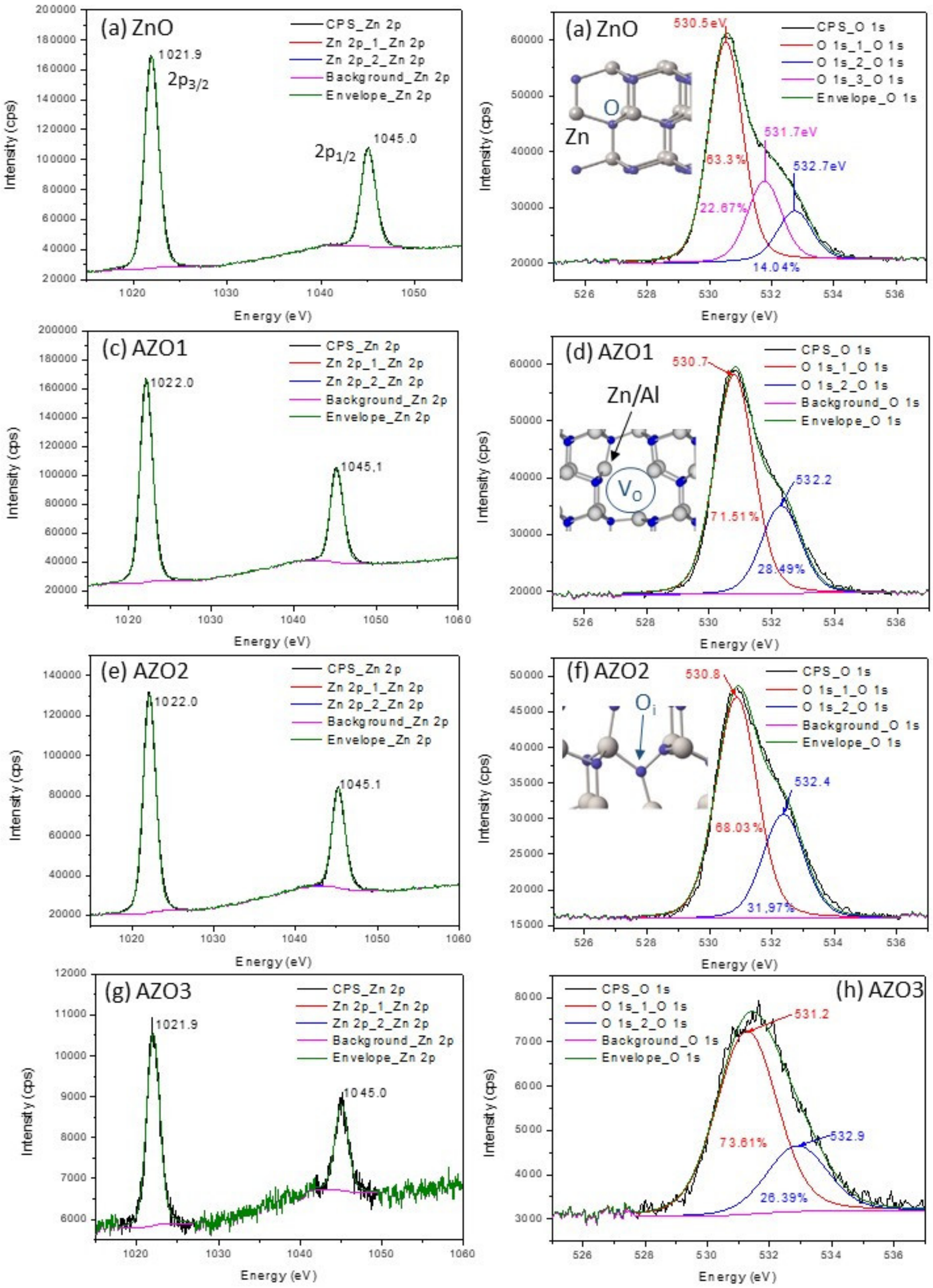

Figure 6. XPS spectra of films deposited for 60 min: (a) and (b): Zn 2p and O 1s of the ZnO film; (c) and (d): Zn 2p and O 1s from the film AZO1; (e) and (f) Zn 2p and O 1s from the AZO2 film; (g) and (h) Zn 2p and O 1s from the AZO3 film.

crystallite size increases for all films. The corresponding SEM images show that the grain size also increases, particularly in the AZO1 sample. The average crystallite size increases for a deposition time of 60 minutes and is even larger for 120 minutes. It is noteworthy that the surface of the AZO1_60 films exhibits larger grain sizes interspersed with smaller grains, while for the AZO1_120 film, these grains are larger and more homogeneous, suggesting growth limited by the average crystallite size, which is larger than that of the other AZO1_30 and AZO1_60 films (Table 2). When the crystallite size is small, there is a larger interface between grains, resulting in higher energy, which can limit grain growth. As the average crystallite size increases, these interfaces decrease, promoting an increase in grain size. Another important correlation involves the lattice parameter *c*. As observed in Table 2, *c* increases for the AZO2 and AZO3 films compared to the ZnO and AZO1 films. This increase in the lattice parameter also limits grain growth, as it can induce internal stresses, increasing dislocation density (δ) and microstrain (ε), for example (Table 2), thereby reducing

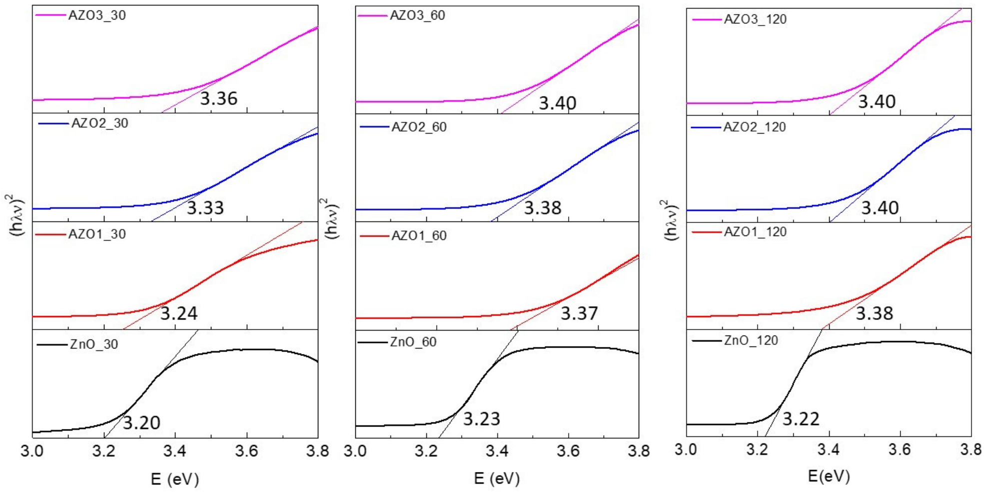

Figure 7. Absorption spectra in the UV-Vis region as a function of the photon energy of films deposited for 30, 60, and 120 min.

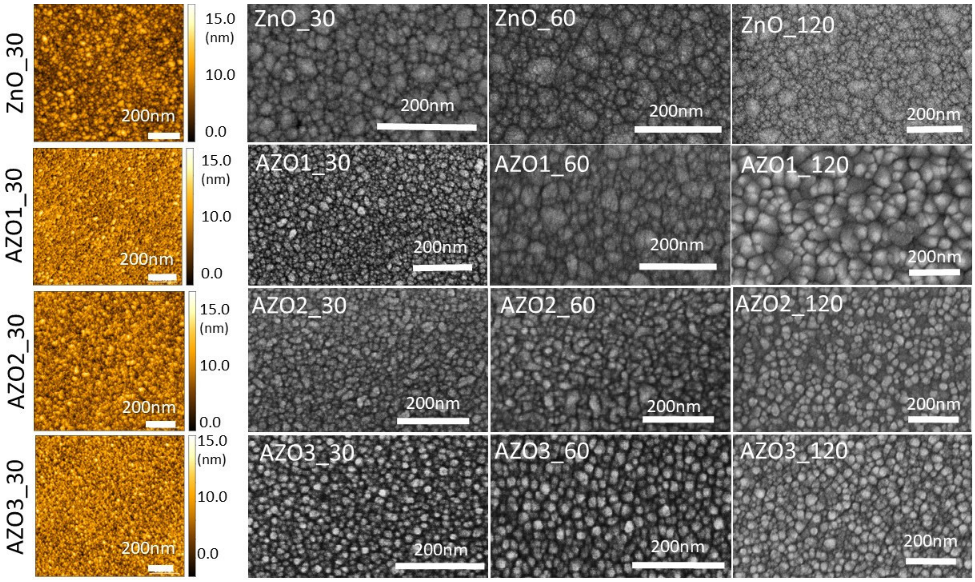

Figure 8. SEM and AFM images of ZnO and AZO films.

crystallite size and even crystallinity, as observed in the intensities of the XRD peaks (Figure 4). These conditions inhibit the continuous growth of grains, as observed in the AZO2 and AZO3 films[62].

Figure 9 shows the sensor response of the films deposited for 30 minutes in the presence of ozone gas (O_3), at concentrations ranging from 50 to 570 ppb, at a working temperature of 250°C. It can be observed that all films are sensitive to different concentrations of O_3 gas. Kang et al.[63] described that the material sensitivity to a particular gas corresponds to an adsorption-oxidation-desorption mechanism between the gas molecules and the material surface comprising the sensor film (such as ZnO and AZO). When exposed to an air atmosphere, O_2 molecules are adsorbed on the surface of ZnO, capturing electrons from its conduction band to form negative oxygen ions. These ions, in turn, become acceptor sites on the material surface. The loss of electrons from the ZnO conduction band creates a depletion region, forming a potential barrier and hindering the movement of electrons between the crystal grains, thus increasing the resistance. When this adsorption process reaches equilibrium, the ZnO resistance becomes constant. By introducing a reducing gas into the system, there will be an electron transfer between the gas molecules and the negative oxygen ions, causing their oxidation. This phenomenon induces a charge transfer process in which additional free electrons migrate back to the ZnO conduction band. As a result, the thickness of the electron depletion layer decreases, the carrier density

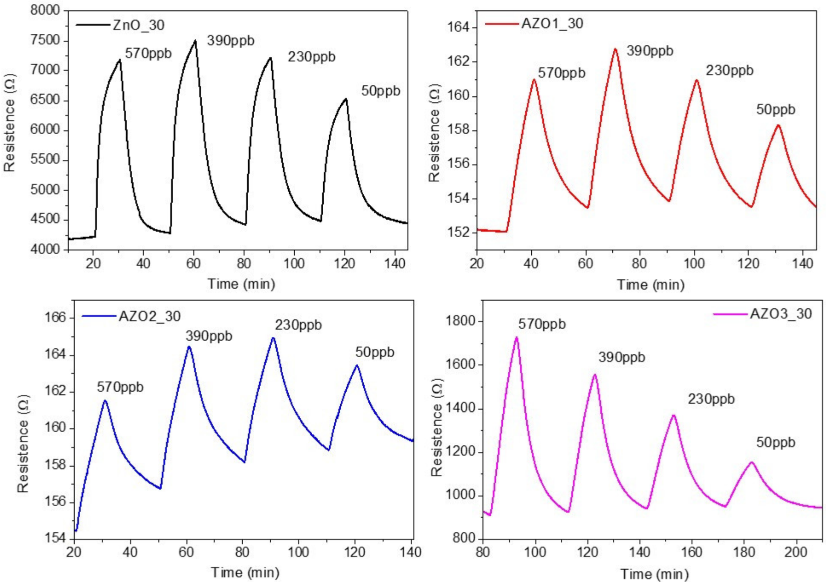

Figure 9. Sensitivity to ozone gas at 250°C presented by ZnO and AZO films deposited in 30 min.

increases, and the ZnO resistance value decreases until equilibrium is reached. From there, with the airflow, the gas gradually separates from the ZnO, and the resistance is restored. Upon encountering an oxidizing gas, such as O_3, the electrons from the ZnO will be captured, reducing the carrier density and increasing the resistance of the material until an equilibrium is reached[63,64]. However, the gas-sensing properties of materials are generally related to both chemical reactions on the surface and gas diffusion. When the temperature is below 150°C, the chemical reaction on the surface plays a predominant role. For temperatures between 150°C and 300°C, both surface chemical reaction and gas diffusion produce a concomitant effect. When the temperature exceeds 300°C, oxygen continues to capture electrons to form oxygen ions, accelerating the chemical reaction on the surface; however, gas diffusion becomes limiting. In this case, the larger the pore size or material porosity, the more favorable the diffusion of gases, and consequently, its sensitivity to the gas will be greater[63,65]. For the case of our ZnO sensor film, the exposure process to O_3 occurred at 250°C, where there were possibly chemical reactions on the film surface and gas diffusion simultaneously.

It can also be observed from Figure 9 that the sensitivity decreases for the Al-doped ZnO films, although the dopant has not changed other characteristics of the material. However, some literature works have shown the opposite of what is observed here, that is, there are reports that a dopant can change the conductivity of ZnO depending on other types of defects. For example, doped ZnO can become more sensitive to atmospheres than undoped ZnO; in other words, there may be an improvement in sensor response with the addition of transition metals[63]. This happens because the presence of the dopant can favor the active adsorption site formation by creating defects such as oxygen vacancies in the host matrix. In the case of the AZO films in this study, these defects are certainly also induced. As observed in the XPS results, regarding the binding energy of O 1s for the films containing Al (Figure 6 (d), (f), and (h)), only two binding energies for oxygen were detected, leading us to consider the generation of oxygen vacancies or interstitial oxygens. This is due to the valence difference between Al^{3+}/Zn^{2+} with the partial substitution of Al^{3+} on the Zn^{2+} site in the ZnO structure. According to Kang et al.[63], defects caused by oxygen vacancies are considered donors, while interstitial oxygens are considered acceptors. The authors suggest that the higher the number of donor defects, the better the sensitivity and detection performance of ZnO to gas, as these defects tend to attract charges from gas molecules, which strongly bond to these defects. In this context, as the Al-doped ZnO films show a decrease in resistance compared to undoped ZnO films, we can hypothesize that there are defects on the surface of the doped films (AZO), predominantly formed by interstitial oxygens (acceptors). This results in a decrease in the concentration of free electrons participating in the adsorption-oxidation-reduction process. However, for the AZO3 film, in addition to defects caused by interstitial oxygens, there may also have been a higher concentration of defects resulting from oxygen vacancies (donors), considering the increased resistance (compared to AZO1 and AZO2) when exposed to O_3 gas, also observed in the undoped ZnO film.

In addition to the oxygen defects present in the AZO films, for gas diffusion reactions to occur, the film must have porosity. As observed in the SEM images (Figure 7), as the Al dopant content increases, there is a tendency for grain size to decrease, resulting in fewer pores. Therefore, another hypothesis for the behavior of these doped samples (AZO1, AZO2, and AZO3) is that the sensitivity to O_3 gas possibly occurs predominantly as a surface phenomenon rather than a volume phenomenon, which explains the decrease in resistance compared to the undoped film (ZnO).

It is important to note that the O_3 gas sensitivity measurement was conducted at a working temperature of 250°C. Although an increase in temperature can help reduce the resistivity of the substrate, which may be advantageous for increasing the carrier concentration in AZO films and enhancing their sensitivity to O_3 gas[50], it is important to highlight that other parameters may negatively influence this sensitivity. The difference in thermal expansion coefficients between the film (ZnO and AZO) and the substrate (Si), for example, can generate significant thermal stresses at the substrate-film interface, which, in turn, can cause deformations in the films. In addition, the difference in lattice parameters between the Si substrate and the AZO films can also contribute to the creation of defects at this interface, such as additional dislocations that may extend to the film surface. These defects may be exacerbated by the presence of Al in the ZnO lattice of the AZO films. Dislocations and other structural defects at the interface can therefore negatively impact the film quality by reducing carrier mobility, affecting the sensor sensitivity and selectivity, leading to changes in gas adsorption on the surface, and altering the electrical response of the AZO films. These defects, generated due to heating of the films to 250°C, can also act as recombination centers for charge carriers, significantly reducing the performance of ZnO-based sensors.

Despite the results showing that the dopant Al impairs the sensitivity of ZnO films, it is clear that it is still possible to detect ozone gas at low concentrations (50 ppb), corresponding to the maximum required by the WHO.

Figure 10 (a) shows the stability of only the ZnO and AZO3 films deposited in 30 minutes during exposure to 50 ppb of ozone gas, while Figure 10 (b), associated with the shaded portion highlighted in the graphs of Figure 10 (a), shows the minimum and maximum resistance of the films, i.e., the resistance at the moment of gas flow opening and closing, respectively, as a function of exposure time. It is observed that both films exhibit good stability at the gas flow opening and interruption moments. The greatest variations occur for the ZnO film, with an increase of 0.3 kΩ from the first to the last cycle of gas flow opening and an increase of 0.4 kΩ for flow closure, also from the first to the last cycle. This result suggests, therefore, that the presence of the dopant Al in the ZnO host lattice contributes to the stability of the film (AZO3) in the presence of O_3 gas.

Figure 11 shows the response, response time, and recovery time of ZnO and AZO films (30 min) exposed to different O_3 gas concentrations. In general, it is observed that the response time increases with the dopant content, ranging between 6.5 and 12 min (Figure 11 (a)). However, there is no significant change as a function of O_3 concentration. On the other hand, the recovery time (Figure 11 (b)) decreases with the Al content, with some exceptions, and also does not follow a rule regarding the variation of O_3 concentration. For this case, the recovery time ranged from 11 to 5 minutes, showing that the ZnO film takes the longest to restore resistance after the O_3 flow interruption. This behavior is directly associated with the resistance variation at the moments of gas flow opening and closing in each cycle, as observed in Figure 10 (b). The values found for the recovery time of the ZnO films are higher than some found in the literature. In the work of Colmenares et al.[66], ZnO films deposited with a ceramic target showed response and recovery times of ~3 min, a value higher than films deposited with metallic Zn targets, also evaluated by the authors. Nagarjuna et al.[67] found response and recovery times of 5 and 10 minutes, respectively, using metallic Zn target for film production. Considering sensor response to O_3 (Figure 11 (c)), the ZnO and AZO3 films are highlighted, showing responses above 30% (> 1.5). These results may be linked to the low porosity of the films, resulting from the ceramic target used, as discussed in the SEM results (Figure 8). In these cases, we can say that there was a predominance of the sensor response on the surface of the films, as opposed to the volume (gas diffusion), which may have influenced the lower sensor response observed when compared to other literature works, such as Nagarjuna et al.[67], who achieved a response value of 216% to O_3 gas. Despite these characteristics, all films in this study were able to detect ozone gas even at low concentrations, as discussed earlier.

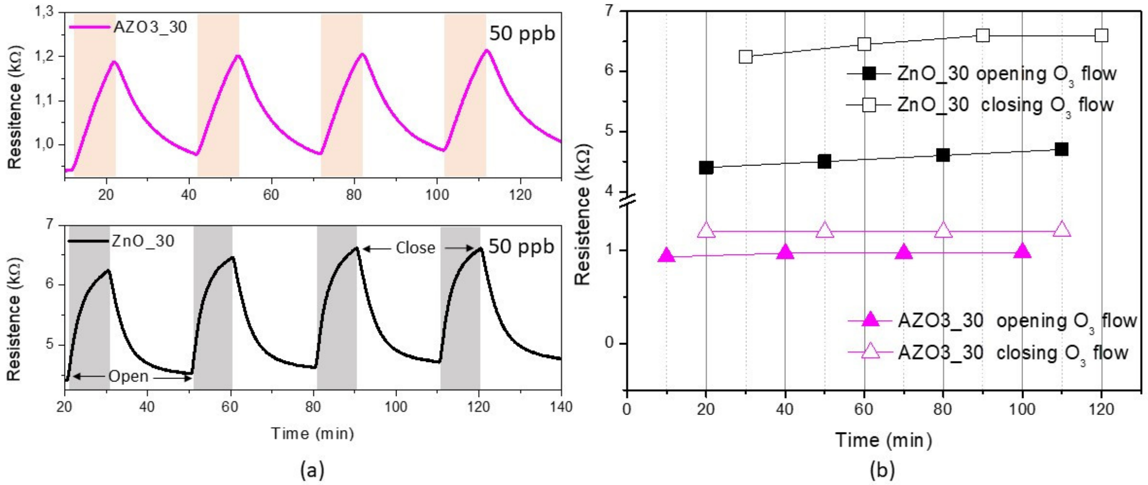

(a) (b)

Figure 10. (a) Stability of ZnO and AZO3 films deposited in 30 min under 50 ppb ozone flow; (b) Resistance associated with opening and closing the ozone gas flow.

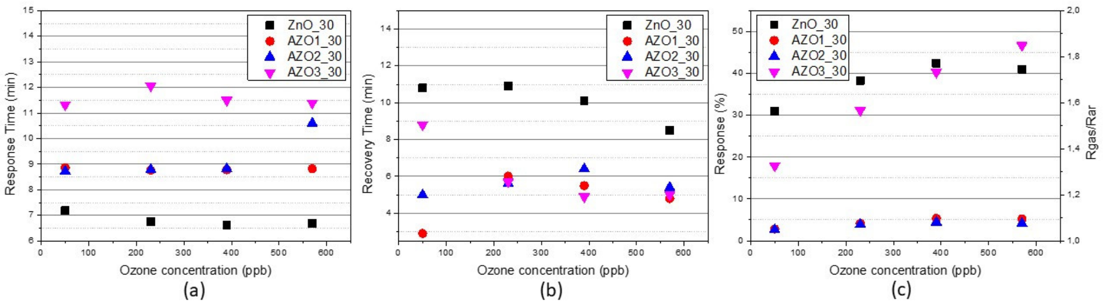

Figure 11. (a) Stability of sensitivity of ZnO and AZO3 films to 50 ppb of ozone gas at 250°C; (b) Response time; and (c) percentage of response of the films as a function of O_3 concentration.

4. Conclusion

The results of this study showed that the ZnO and AZO ceramic targets production by SSR is feasible, considering their physical characteristics such as the density and crystallinity of the desired phases. The targets were satisfactorily used for the deposition of thin films via magnetron sputtering. All obtained films showed preferential growth on the lowest energy plane of wurtzite. The presence of Al in the ZnO lattice was confirmed by XPS characterizations. The physical and morphological characteristics of the films were influenced by the deposition time, with increasing thickness and decreasing grain size, without altering the energy gap over time. Sensitivity to O_3 gas results showed that Al-doping ZnO impairs such sensitivity, which may be associated with the presence of defects caused by interstitial oxygen or increased densification of the films. Despite the decrease in sensitivity to O_3, it is still possible to detect it at low concentrations, such as 50 ppb, with all films. These results demonstrate that thin films of ZnO and Al-doped ZnO are efficient in detecting ozone gas, even at the lowest concentrations established as the maximum limit without health hazards according to the WHO.

5. Acknowledgments

The authors thank the Laboratory at the Brazilian Nanotechnology National Laboratory (LNNano, Proposal 20233328 and 20233050), Campinas, SP, Brazil, and FAPESP-CEPID (Process 2013/07296-2).

6. References

1. Hong JS, Matsushita N, Kim KH. Effect of dopants and thermal treatment on properties of Ga-Al-ZnO thin films fabricated by hetero targets sputtering system. Thin Solid Films. 2013;531:238-42. http://doi.org/10.1016/j.tsf.2013.01.089.
2. Ramadan R, Dadgostar S, Manso-Silván M, Pérez-Casero R, Hernandez-Velez M, Jimenez J, et al. Silver-enriched ZnO:Ag thin films deposited by magnetron co-sputtering: Post annealing effects on structural and physical properties. Mater Sci Eng B. 2022;276:115558. http://doi.org/10.1016/j.mseb.2021.115558.
3. Gomes L, Marques A, Branco A, Simões M, Cardoso S, Silva F, et al. IZO deposition by RF and DC sputtering on paper and application on flexible electrochromic devices. Displays. 2013;34:326-33. http://doi.org/10.1016/j.displa.2013.06.004.
4. Woo K, Lee SH, Lee S, Bak S-Y, Kim Y-J. Effect of interfacial InZnO conducting layer on electrical performance and bias stress stability of InAlZnO thin-film transistors. Microelectron Eng. 2019;215:111006-1-4. http://doi.org/10.1016/j.mee.2019.111006.
5. Kim H-J, Seo K-W, Noh Y-J, Na S-I, Sohm A, Kim D-W, et al. Work function and interface control of amorphous IZO electrodes by MoO_3 layer grading for organic solar cells. Sol Energy Mater Sol Cells. 2015;141:194-202. http://doi.org/10.1016/j.solmat.2015.05.036.
6. Li X, Zhang H, Lu X, Fang Z, Yao R, Wang Y, et al. Effect of oxygen pressure on GZO film as active layer of the TFT fabricated at room temperature. Superlattices Microstruct. 2020;137:106317. http://doi.org/10.1016/j.spmi.2019.106317.
7. Peng S, Yao T, Yang Y, Zhang K, Jiang J, Jin K, et al. Influences of the RF power ratio on the optical and electrical properties of GZO thin films by DC coupled RF magnetron sputtering at room temperature. Physica B. 2016;503:111-6. http://doi.org/10.1016/j.physb.2016.09.027.
8. Tseng S-F. Investigation of post-annealing aluminum-doped zinc oxide (AZO) thin films by a graphene-based heater. Appl Surf Sci. 2018;448:163-7. http://doi.org/10.1016/j.apsusc.2018.04.036.
9. García-Salinas F, Vázquez-Durán A, Yáñez-Limón JM. Comparative study of Al-doped ZnO films deposited by sol–gel and by sputtering using asintered target from ZnO nanoparticles synthesized by sol–gel. Bol Soc Esp Ceram Vidr. 2023;62(2):134-44. http://doi.org/10.1016/j.bsecv.2021.11.004.
10. Singh M, Ambedkar AK, Tyagi S, Kumar V, Yadav P, Kumar A, et al. Room temperature photoluminescence and spectroscopic ellipsometry of reactive co-sputtered Cu-doped ZnO thin films. Optik (Stuttg). 2022;257:168860. http://doi.org/10.1016/j.ijleo.2022.168860.
11. Catto AC, Silva LF, Bernardi MIB, Bernardini S, Aguir K, Longo E, et al. Local structure and surface properties of $Co_xZn_{1-x}O$ thin films for ozone gas sensing. ACS Applied Materials & Interfaces. 2016;8:26066. http://doi.org/10.1021/acsami.6b08589.
12. Petrov VV, Ignatieva IO, Volkova MG, Gulyaeva IA, Pankov IV, Bayan EM. Polycrystalline transparent Al-Doped ZnO Thin films for photosensitivity and optoelectronic applications. Nanomaterials (Basel). 2023;13(16):2348. http://doi.org/10.3390/nano13162348.
13. Liu Y, Zeng Q, Nie C, Yu HF. Mg and Ga co-doped ZnO transparent conductive thin films by dual- target magnetron sputtering: Fabrication, structure, and characteristics. J Alloys Compd. 2022;907:164480. http://doi.org/10.1016/j.jallcom.2022.164480.
14. Goktas A, Aslana F, Yeşilatab B, Boza I. Physical properties of solution processable n-type Fe and Al co-doped ZnO nanostructured thin films: role of Al doping levels and annealing. Mater Sci Semicond Process. 2018;75:221-33. http://doi.org/10.1016/j.mssp.2017.11.033.
15. Kang H, Lu Z, Zhong Z, Gu J. Structural, optical and electrical characterization of Ga-Mg co-doped ZnO transparent conductive

films. Mater Lett. 2018;215:102-5. http://doi.org/10.1016/j.matlet.2017.12.072.

16. Ali D, Muneer I, Butt MZ. Influence of aluminum precursor nature on the properties of AZO thin films and its potential application as oxygen sensor. Opt Mater. 2021;120:111406. http://doi.org/10.1016/j.optmat.2021.111406.
17. Kathwate LH, Umadevi G, Kulal PM, Nagaraju P, Dubal DP, Nanjundan AK, et al. Ammonia gas sensing properties of Al doped ZnO thin films. Sens Actuators A Phys. 2020;313:112193. http://doi.org/10.1016/j.sna.2020.112193.
18. Aydin E, Sankir ND. AZO/metal/AZO transparent conductive oxide thin films for spray pyrolyzed copper indium sulfide based solar cells. Thin Solid Films. 2018;653:29-36. http://doi.org/10.1016/j.tsf.2018.03.012.
19. Al Farsi B, Souier TM, Al Marzouqi F, Al Maashani M, Bououdina M, Widatallah HM, et al. Structural and optical properties of visible active photocatalytic Al doped ZnO nanostructured thin films prepared by dip coating. Opt Mater. 2021;113:110868. http://doi.org/10.1016/j.optmat.2021.110868.
20. Nebatti A, Pflitsch C, Curdts B, Atakan B. Using the acetylacetonates of zinc and aluminium for the Metalorganic Chemical Vapour Deposition of aluminium doped zinc oxide films. Mater Sci Semicond Process. 2015;39:467-75. http://doi.org/10.1016/j.mssp.2015.05.053.
21. Chergui ANE, Pflitsch C, Atakan B. Atmospheric pressure metal-organic chemical vapor deposition (AP-MOCVD) growth of undoped and aluminium-doped ZnO thin film using hot wall reactor. Surf Interfaces. 2021;22:100883. http://doi.org/10.1016/j.surfin.2020.100883.
22. Liu Y, Lian J. Optical and electrical properties of aluminum-doped ZnO thin films grown by pulsed laser deposition. Appl Surf Sci. 2007;253:3727-30. http://doi.org/10.1016/j.apsusc.2006.08.012.
23. Xia Y, Wang P, He G, Zhang M, Shi S, Liu Y, et al. Microstructure, opotoelectrical and pre-strain dependent electrical properties of AZO films on flexible glass substrates for flexible electronics. Surf Coat Tech. 2017;320:34-8. http://doi.org/10.1016/j.surfcoat.2017.02.014.
24. Mbule P, Wang D, Grieseler R, Schaaf P, Muhsin B, Hoppe H, et al. Aluminum-doped ZnO thin films deposited on flat and nanostructured glass substrates: quality and performance for applications in organic solar cells. Sol Energy. 2018;172:219-24. http://doi.org/10.1016/j.solener.2018.03.007.
25. Pat S, Mohammadigharehbagh R, Ozen S, Senay V, Yudar HH, Korkmaz S. The Al doping effect on the surface, optical, electrical and nanomechanical properties of the ZnO and AZO thin films prepared by RF sputtering technique. Vacuum. 2017;141:210-5. http://doi.org/10.1016/j.vacuum.2017.04.025.
26. Bose S, Arokiyadoss R, Bhargav PB, Ahmad G, Mandal S, Barua AK, et al. Modification of surface morphology of sputtered AZO films with the variation of the oxygen. Mater Sci Semicond Process. 2018;79:135-43. http://doi.org/10.1016/j.mssp.2018.01.027.
27. Subramanyam TK, Goutham P, Pavan Kumar S, Yadhuraj SR, Geetha KS. Optimization of sputtered AZO thin films for device application. Mater Today Proc. 2018;5:10851-9. http://doi.org/10.1016/j.matpr.2017.12.373.
28. Lee M, Park Y, Kim K, Hong J. Influence of sputtering conditions on the properties of aluminum-doped zinc oxide thin film fabricated using a facing target sputtering system. Thin Solid Films. 2020;703:137980. http://doi.org/10.1016/j.tsf.2020.137980.
29. Kumar MK, Raj PD, Jeyadheepan K, Sridharan M. Effect of Aluminum doping on the properties of magnetron sputtered ZnO films. Mater Today Proc. 2016;3:1525-30. http://doi.org/10.1016/j.matpr.2016.04.037.
30. Stamate E. Lowering the resistivity of aluminum doped zinc oxide thin films by controlling the self-bias during RF magnetron sputtering. Surf Coat Tech. 2020;402:126306. http://doi.org/10.1016/j.surfcoat.2020.126306.
31. Shi F. Magnetron Sputtering. London: InTechOpen; 2018. Introductory Chapter: Basic Theory of Magnetron Sputtering; p. 1-4. http://doi.org/10.5772/intechopen.80550
32. Braüer G, Szyszka B, Vergöhl M, Bandorf M. Magnetron sputtering–Milestones of 30 years. Vacuum. 2010;84:1354-9. http://doi.org/10.1016/j.vacuum.2009.12.014.
33. Goktas S, Tumbul A, Goktas A. Growth technique–induced highly CAxisoriented ZnO:Mn, ZnO:Fe and ZnO:Co thin films: a comparison of nanostructure, surface morphology, optical band gap, and room temperature ferromagnetism. J Supercond Nov Magn. 2023;36:1875-92. http://doi.org/10.1007/s10948-023-06630-4.
34. Huang HS, Tung HC, Chiu CH, Hong IT, Chen RZ, Chang TJ, et al. Highly conductive alumina-added ZnO ceramic target prepared by reduction sintering and its effects on the properties of deposited thin films by direct current magnetron sputtering. Thin Solid Films. 2010;518:6071-5. http://doi.org/10.1016/j.tsf.2010.06.004.
35. Wei T, Zhang Y, Yang Y, Tan R, Cui P, Song W. Effects of ZnAl2O4 segregation in high temperature sintered Al-doped ZnO sputtering target on optical and electrical properties of deposited thin films. Surf Coat Tech. 2013;221:201-6. http://doi.org/10.1016/j.surfcoat.2013.01.049.
36. Asemi M, Ahmadi M, Ghanaatshoar M. Preparation of highly conducting Al-doped ZnO target by vacuum heat-treatment for thin film solar cell applications. Ceram Int. 2018;44:12862-8. http://doi.org/10.1016/j.ceramint.2018.04.096.
37. Regmi G, Velumani S. Impact of target power on the properties of sputtered intrinsic zinc oxide(i-ZnO) thin films and its thickness dependence performance on CISe solar cells. Opt Mater. 2021;119:111350. http://doi.org/10.1016/j.optmat.2021.111350.
38. Kalvania PR, Shapouria S, Jahangiria AR, Jalili YS. Microstructure evolution in high density AZO ceramic sputtering target fabricated via multistep sintering. Ceram Int. 2020;46(5):5983-92. http://doi.org/10.1016/j.ceramint.2019.11.053.
39. Korotcenkov G, Cho BK. Ozone measuring: what can limit application of SnO2-based conductometric gas sensors? Sens Actuators B Chem. 2012;161:28-44. http://doi.org/10.1016/j.snb.2011.12.003.
40. Wood DL, Tauc J. Weak absorption tails in amorphous semiconductors. Phys Rev B Condens Matter Mater Phys. 1972;5:3144-51. http://doi.org/10.1103/PhysRevB.5.3144.
41. Vlassov S, Bocharov D, Polyakov B, Vahtrus M, Šutka A, Oras S, et al. Critical review on experimental and theoretical studies of elastic properties of wurtzitestructured ZnO nanowires. Nanotechnol Rev. 2023;12:20220505. http://doi.org/10.1515/ntrev-2022-0505.
42. Mohanty P, Mohapatro S, Mahapatra R, Mishra DK. Low cost synthesis route of spinel ZnAl2O4. Mater Today Proc. 2021;35:130-2. http://doi.org/10.1016/j.matpr.2020.03.508.
43. Srinatha N, Satyanarayana Reddy S, Suriyamurthy N, Rudresh Kumar KJ, Suresh Kumar MR, Madhu A, et al. New fuel governed combustion synthesis and improved luminescence in nanocrystalline Cr3+ doped ZnAl2O4 particles. Results in Optics. 2022;8:100242. http://doi.org/10.1016/j.rio.2022.100242.
44. Jin Q, Wang S, Lei C, Liu S, Feng S, Ma T, et al. ZnAl2O4/sulfur-doped g-C3N4 S-scheme heterojunction for efficient photocatalytic degradation of malachite green. Opt Mater. 2023;136:113488. http://doi.org/10.1016/j.optmat.2023.113488.
45. Fang G, Li D, Yao B-L. Fabrication and characterization of transparent conductive ZnO:Al thin films prepared by direct current magnetron sputtering with highly conductive ZnO(ZnAl2O4) ceramic target. J Cryst Growth. 2003;247:393-400. http://doi.org/10.1016/S0022-0248(02)02012-2.
46. Mallick A, Kole A, Ghosh T, Chaudhuri P, Basak D. Zinc aluminate spinel impurity phase in Al doped ZnO ceramic target

and pulsed laser ablated films: curse or blessing? Sol Energy. 2014;108:80-7. http://doi.org/10.1016/j.solener.2014.05.049.

47. Wang X-M, Bai X, Duan H-Y, Shi Z-X, Sun J, Lu S-G, et al. Preparation of Al-doped ZnO sputter target by hot pressing. Trans Nonferrous Met Soc China. 2011;21:1550-6. http://doi.org/10.1016/S1003-6326(11)60895-9.
48. Liu X, Sun B, Zeng X, Zuo Z, Zhang W, Wang Z, et al. Effects of Al_2O_3 doping on the microstructural evolution and densification process of AZO targets. Ceram Int. 2022;48:16196-205. http://doi.org/10.1016/j.ceramint.2022.02.167.
49. Tang P, Li B, Feng L. The optical and electrical properties of ZnO: al thin films deposited at low temperatures by RF magnetron sputtering. Ceram Int. 2018;44(4):4154-7. http://doi.org/10.1016/j.ceramint.2017.11.216.
50. Wen R, Wang L, Wang X, Yue G-H, Chen Y, Peng D-L. Influence of substrate temperature on mechanical, optical and electrical properties of ZnO:Al films. J Alloys Compd. 2010;508:370-4. http://doi.org/0.1016/j.jallcom.2010.08.034.
51. Aba Z, Goktas A, Kilic A. Characterization of Zn1-xLaxS thin films; compositional, surface, optical, and photoluminescence properties for possible optoelectronic and photocatalytic applications. J Sol-Gel Sci Technol. 2024;109:260-71. http://doi.org/10.1007/s10971-023-06273-w.
52. Das A, Das G, Kabiraj D, Basak D. High conductivity along with high visible light transparency in Al implanted sol-gel ZnO thin film with an elevated figure of merit value as a transparent conducting layer. J Alloys Compd. 2010;835:155221. http://doi.org/10.1016/j.jallcom.2020.155221.
53. Cullity BD, Stock CK. Elements of X-ray diffraction. 3rd ed. London: Pearson Education Limited; 2014.
54. Kurtaran S. Al doped ZnO thin films obtained by spray pyrolysis technique: influence of different annealing time. Opt Mater. 2021;114:110908. http://doi.org/10.1016/j.optmat.2021.110908.
55. Namgung G, Ta QTH, Yang W, Noh J-S. Diffusion-driven Al-Doping of ZnO nanorods and stretchable gas sensors made of doped ZnO Nanorods/Ag Nanowires bilayers. Appl. Mater. Interfaces. 2019;11:1411-9. http://doi.org/10.1021/acsami.8b17336.
56. Girija KG, Shaheera M, Somasundaram K. Correlating the properties of RF sputtered ZnO nanocrystalline films deposited using sintered and powder targets. Nano-Structures & Nano-Objects. 2021;26:100758. http://doi.org/10.1016/j.nanoso.2021.100758.
57. Tsai SH, Ho TS, Jhuo HJ, Ho CR, Chen SA, He J-H. Toward high efficiency of inverted organic solar cells: concurrent improvement in optical and electrical properties of electron transport layers. Appl Phys Lett. 2013;102:253111. http://doi.org/10.1063/1.4812981.
58. Ochoa-Martínez E, Navarrete-Astorga E, Ramos-Barrado J, Gabás M. Evolution of Al:ZnO optical response as a function of doping level. Appl Surf Sci. 2017;421:680-6. http://doi.org/10.1016/j.apsusc.2016.10.103.
59. Sholeha N, Afianti AM, Diantoro M, Aripriharta A, Pujiarti H. Structure, functional groups, and optical properties of Al doped ZnO nanorods thin films. Mater Today Proc. In press. http://doi.org/10.1016/j.matpr.2023.04.159.
60. Al-Ghamdi AA, Al-Hartomy OA, El Okr M, Nawar AM, El-Gazzar S, El-Tantawy F, et al. Semiconducting properties of Al doped ZnO thin films. Spectrochim Acta A Mol Biomol Spectrosc. 2014;131:512-7. http://doi.org/10.1016/j.saa.2014.04.020.
61. Pawar P, Jha PK, Panda SK, Jha PA, Singh P. Band-Gap engineering in ZnO thin films: a combined experimental and theoretical study. Phys Rev Appl. 2018;9:054001. http://doi.org/10.1103/PhysRevApplied.9.054001.
62. Goktas A. Role of simultaneous substitution of Cu2+ and Mn2+ in ZnS thin films: defects-induced enhanced room temperature ferromagnetism and photoluminescence. Physica E. 2020;117:113828. http://doi.org/10.1016/j.physe.2019.113828.
63. Kang Y, Yu F, Zhang L, Wang W, Chen L, Li Y. Review of ZnO-based nanomaterials in gas sensors. Solid State Ion. 2021;360:115544. http://doi.org/10.1016/j.ssi.2020.115544.
64. Yoon Y, Truong PL, Lee D, Ko SH. Metal-Oxide nanomaterials synthesis and applications in flexible and wearable sensors. ACS Nanosci. Au. 2022;2:64-92. http://doi.org/10.1021/acsnanoscienceau.1c00029.
65. Franco MA, Conti PP, Andre RS, Correa DS. A review on chemiresistive ZnO gas sensors. Sensors and Actuators Reports. 2022;4:100100. http://doi.org/10.1016/j.snr.2022.100100.
66. Colmenares YN, Correr W, Lima BS, Mastelaro VR. The effect of morphology on the ozone-gas sensing properties of zinc oxide sputtered films. Thin Solid Films. 2020;703:137975. http://doi.org/10.1016/j.tsf.2020.137975.
67. Nagarjuna Y, Hsiao Y-J, Wang S-C, Shao C-Y, Huang Y-C. Nanoporous ZnO structure prepared by HiPIMS sputtering for enhanced ozone gas detection. Mater Today Commun. 2023;35:106024. http://doi.org/10.1016/j.mtcomm.2023.106024.